

Electromagnetic Energy Extraction from Kerr Black Holes: Ab-Initio Calculations

Claudio Meringolo¹, Filippo Camilloni¹, and Luciano Rezzolla^{1,2,3}

¹ Institut für Theoretische Physik, Goethe Universität, Max-von-Laue-Str. 1
Frankfurt am Main, 60438, Germany

² CERN, Theoretical Physics Department, Geneva, 1211, Switzerland

³ School of Mathematics, Trinity College, Dublin, Ireland

Abstract

The possibility of extracting energy from a rotating black hole via the Blandford-Znajek mechanism represents a cornerstone of relativistic astrophysics. We present general-relativistic collisionless kinetic simulations of Kerr black-hole magnetospheres covering a wide range in the black-hole spin. Considering a classical split-monopole magnetic field, we can reproduce with these ab-initio calculations the force-free electrodynamics of rotating black holes and measure the power of the jet launched as a function of the spin. The Blandford-Znajek luminosity we find is in very good agreement with analytic calculations and compatible with general-relativistic magnetohydrodynamics simulations via a simple rescaling. These results provide strong evidence of the robustness of the Blandford-Znajek mechanism and accurate estimates of the electromagnetic luminosity to be expected in those scenarios involving rotating black holes across the mass scale.

Introduction

A rotating (or Kerr) black hole (BH) has a reservoir of rotational energy that can be tapped to drive ultrarelativistic jets if the BH is embedded in a magnetic field. This mechanism, first proposed by Blandford and Znajek (BZ) [1] could be at work in accreting BHs across the mass scale, i.e., either in supermassive BHs where it would be responsible for the phenomenology of Active Galactic Nuclei (AGNs) or in stellar-mass BHs, where it could represent the engine powering gamma-ray bursts (GRBs; see, e.g., [2]). What these apparently different scenarios have in common is the presence of electromagnetic (EM) fields building up a magnetosphere and of a force-free plasma permeating it.

Over the last decades, an enormous literature has been built to describe and validate the BZ mechanism, either analytically [1, 3–9], via general-relativistic magnetohydrodynamic (GRMHD) simulations [10–26], or using more fundamental particle-based, relativistic simulations [27–32]. The two numerical approaches have distinct advantages, with the fluid nature of the former ones being particularly suited to provide a global and large-scale description of the launching of magnetically dominated jets and the kinetic nature of the latter being more effective in reproducing the physical conditions expected in BH magnetospheres, where the plasma is closer to a force-free regime. Both approaches, however, have had the merit of confirming the plausibility of the BZ mechanism under a variety of conditions.

Exploiting a newly developed general-relativistic particle-in-cell (GRPIC) numerical code, `FPIC`, we present the first and most comprehensive campaign of fully kinetic, two-dimensional simulations of force-free BH magnetospheres. Using as a reference the classic split-monopole proposed by Blandford and Znajek [1], we simulate the highly dynamic current sheet that forms in the equatorial plane and that leads to a rich and powerful process of magnetic reconnection [28, 33, 34]. The latter occurs through the development of the tearing instability, so that a chain of plasmoids forms along the reconnection layer, which are ejected at relativistic velocities [35, 36]. Our analysis allows us to characterise the magnetic-reconnection rate and to express it analytically in terms of the distance from the event horizon and of the BH spin. More importantly, we quantify the extraction of rotational energy from the BH to the EM fields and particles via the BZ mechanism and compare it with the original lowest-order expression by Blandford and Znajek [1], with more recent high-order analytic expressions [9], and

with GRMHD simulations [14]. In addition to finding a surprisingly good agreement between the results of the GRPIC simulations and the high-order analytic estimates, we discuss how the GRMHD results can also be recovered via a simple rescaling that depends only on the effective magnetic-field topology. Finally, we show that populations of particles with negative energy at infinity are present inside the ergosphere, suggesting that also the Penrose process is active [37–40].

Results

Overview of the Simulations

Since the BH mass M plays here only the role of a scaling factor, the typical scenario characterising a force-free magnetosphere around rotating BH in general relativity is described by a single parameter, namely, the dimensionless BH spin $a_* := J_*/M^2$, where J_* is the spin angular momentum of the Kerr spacetime. Furthermore, since we are here interested to perform a systematic study of the dynamics of charged particles and EM fields in this scenario, we have carried out twelve, high-resolution, kinetic GRPIC simulations differing in the dimensionless BH spin (see Tab. 1 for a summary of the simulations). While they have represented a significant computational cost, the campaign of simulations has been essential to obtain a clear and comprehensive description.

The details of the numerical code employed for the simulations are briefly summarised in the [Methods](#) section below, but it is important to recall here that all simulations are initiated in electrovacuum, i.e., in the absence of charged particles, and share the same initial seed magnetic field given by a split-monopole, solution of the Maxwell equations in the electrovacuum Schwarzschild spacetime. In this case, using spherical coordinates, the radial component of the magnetic field as measured by a fiducial observer (FIDO) is given by $B^r := \partial_\theta \Psi / \sqrt{\gamma}$, where γ is the determinant of the spatial three-metric γ_{ij} , while $\Psi(r, \theta)$ is the gauge-invariant magnetic-flux function $\Psi(r, \theta) = 4M^2 B_0 \zeta(\theta)(1 - \cos \theta)$. The factor $\zeta(\theta)$ is introduced to model the equatorial current-sheet necessary to sustain the field discontinuity [41]. We note that, in ideal conditions, one would consider a step-function $\zeta = 2\mathcal{H}(\theta - \pi/2) - 1$, where $\mathcal{H}(x)$ is the Heaviside function. In practice, we employ the smooth function $\zeta := 2/\pi \arctan[\chi(\theta - \pi/2)]$ with χ controlling the jump and fixed at $\chi = 1000$.

In all simulations, the initial magnetic-field strength B_0 is specified in terms of the dimensionless field $\tilde{B}_0 := r_g/r_L = GM e B_0 / (m_e c^4)$ where $r_g := GM/c^2$ is the gravitational radius, $r_L := m_e c^2 / (e B_0)$ is the Larmor radius, and m_e, e are the reference electron mass and charge, respectively. Following [27], we set $\tilde{B}_0 = 10^3$, which is equivalent to a magnetic field of $\simeq 1$ G for a BH of mass $M \simeq 10 M_\odot$ (or of $\simeq 10^{-5}$ G for a BH with the mass of Sgr A*, i.e., $M \simeq 10^6 M_\odot$). While these fields are admittedly not realistic, they keep the computational costs affordable in our extensive spin exploration and represent a common choice [27, 32].

The value of B_0 also provides a reference scale for a number of plasma-related quantities, such as the Goldreich-Julian number density $n_{\text{GJ}} := \Omega_h B_0 / (4\pi c e)$ [42], which measures the minimum number density required to screen the longitudinal components of the electric field, and where Ω_h is the angular velocity of the event horizon (clearly, higher values of \tilde{B}_0 would force the use of a larger number of particles). Our setup also preserves the important hierarchy of astrophysical scales, both in space, i.e., $r_L \ll d_p \ll r_g$, and in time, i.e., $\Omega_h \ll \omega_p \ll \omega_L$, where $d_p := c/\omega_p$ is the plasma skin depth, $\omega_p := \sqrt{4\pi n_{\text{GJ}} e^2 / (m_e c^2)}$ is the plasma frequency, and $\omega_L := c/r_L$ the Larmor frequency. Hereafter, and unless specified differently, we use geometrised units in which $c = 1 = G$, with c and G the speed of light and the gravitational constant, respectively.

In the presence of spacetime rotation, the initial static Schwarzschild split-monopole evolves towards a stationary electrovacuum configuration that preserves a monopolar topology in the poloidal plane and an equatorial current-sheet, while exhibiting gravitationally-induced toroidal magnetic fields, as well as electric fields along the magnetic-field lines. These gravitationally induced EM fields are similar to what observed in the Wald solution [43] as considered, for instance, in [27, 44, 45].

After the vacuum EM fields settle to a stationary configuration at $t = t_{\text{inj}} = 50 M$, a e^-/e^+ -pair plasma is injected in the spherical volume with coordinate radius $r_h < r < 15 M$, where $r_h := (1 + \sqrt{1 - a_*^2}) M$ marks the location of the event horizon. This particle injection, that is customary in PIC simulations, is repeated for all subsequent times $\bar{t} := t - t_{\text{inj}} > 0$ and it is necessary to establish a plasma-filled magnetosphere in which the electric-field components longitudinal to the magnetic-field are screened by the plasma. Furthermore, in order for the magnetosphere to attain the force-free regime in which the inertial and thermal contributions of the particles to the total energy-and-momentum balance are smaller than those associated with the magnetic

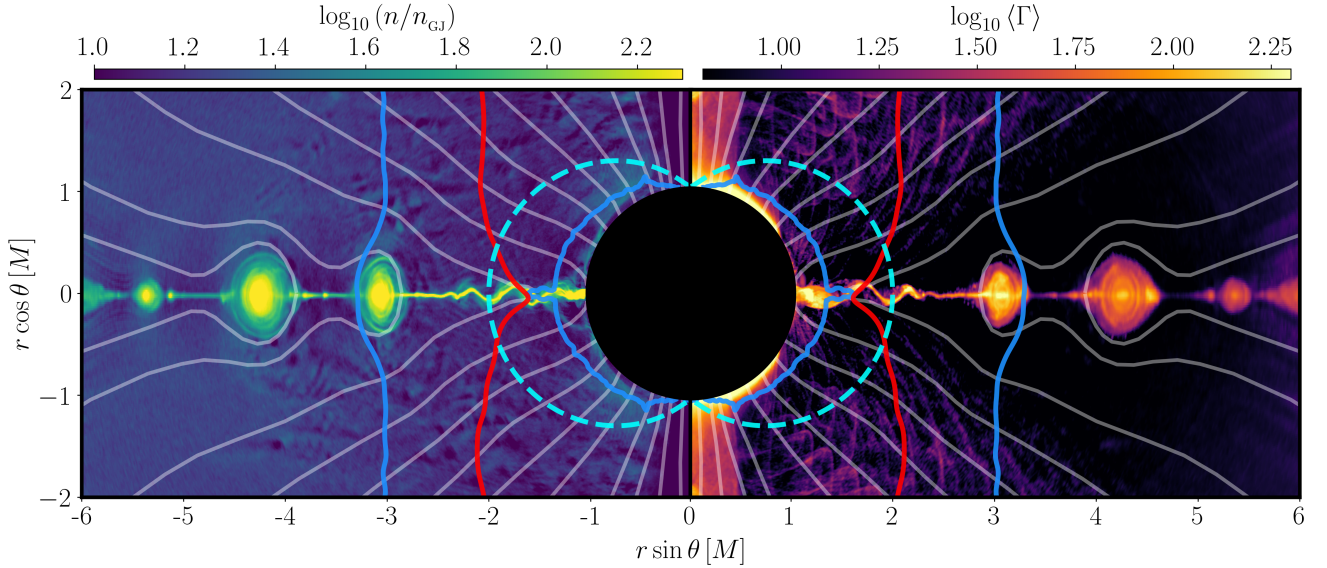


Figure 1: *Left panel:* Total number density of particles normalised to the Goldreich-Julian density n/n_{GJ} as measured by a FIDO observer. The data refers to time $\bar{t} = 10 M$ and to a BH with spin $a_* = 0.999$. Also shown are the ergosphere (cyan dashed line), the inner and outer light surfaces (blue solid lines), and the stagnation surface (red solid line). *Right panel:* the same as on the left for but for the Lorentz factor Γ .

field, the condition for the plasma replenishment is expressed as $n < \mathcal{M} n_{\text{GJ}}$ [46], where n is the total number density $n := n_{e^-} + n_{e^+}$, and n_{e^-}, n_{e^+} the number densities of electrons and positrons, respectively. The factor $\mathcal{M} > 1$ is the so-called multiplicity that we set to $\mathcal{M} = 10$ so as to have an accurate representation of the BH magnetosphere. We have verified that, in this way, the highly magnetised magnetosphere in our simulations obeys $\sigma = B_i B^i / (4\pi n m_e) \gg \Gamma$ [46], where σ is the magnetisation parameter, and Γ the Lorentz factor relative to the FIDO; typical values in our simulations are $\sigma \simeq 100$ and $\sigma/\Gamma \gtrsim 10$.

The particles are injected in each cell with FIDO-frame velocities randomly drawn from a relativistic Maxwell–Jüttner of dimensionless temperature $\Theta := k_B T / m_e = 0.5$, with k_B being the Boltzmann constant. Furthermore, to increase the density of particles near the equatorial region, we modulate the injected number density with a simple polar profile $n_{\text{inj}} = n_0 \sin(\theta)$, where the values of n_0/n_{GJ} depend on the spin and can be found in Tab. 1. We have checked that other injection methods, e.g., using the local parallel electric field as a proxy for the electron-positron discharge [27, 47], lead to results that are qualitatively and quantitatively similar.

Plasmoid formation and dynamics

Figure 1 offers a representative view at time $\bar{t} = 10 M$ of the most extreme of our configurations, namely, of a Kerr BH with spin $a_* = 0.999$ (see case a. 999 in Tab. 1). In particular, shown in the left panel of Fig. 1 is the distribution of the total particle number density normalised to the Goldreich-Julian value n_{GJ} . Note the presence on the equatorial plane of a current sheet – where the poloidal magnetic field inverts its polarity – and of a series of plasmoids – i.e., confined plasma concentrations – moving either to larger radii or towards the BH horizon. Furthermore, the colormap reveals that the number density along the current sheet and inside the plasmoids is on average at least one order of magnitude larger than elsewhere in the computational domain. Also shown with thin grey lines are the projections of the magnetic-field lines over the poloidal plane, which preserve the overall split-monopole topology despite the appearance of polar and azimuthal components. We recall, in fact, that when the system reaches force-free quasi-stationary conditions, the magnetic-field lines rotate rigidly with an angular velocity $\Omega_f = -E_\theta / (\sqrt{\gamma} B^r)$, that approximates the value expected for a split-monopole topology, $\Omega_f \simeq \Omega_h/2$ [1, 11, 19]. At the same time, the toroidal magnetic field respects the Znajek regularity condition at the horizon, $B_\phi = \sqrt{\gamma} [\beta^r D^\theta + \sin \theta \sqrt{\gamma} (\Omega_f - \Omega_h) B^r]$ [1, 9, 48, 49], where β^r is the shift vector and D is the electric field measured by the FIDO [11] (see Methods for details), and reverses polarity across the equator.

Also shown in Fig. 1 is the region inside the outer event horizon r_+ (black-shaded area) and the position of the ergosphere, or static limit, r_0 (cyan dashed line). We recall that under axisymmetry and force-free quasi-stationarity, surfaces of superluminal rotation appear for the magnetic-field lines and corresponding to the two

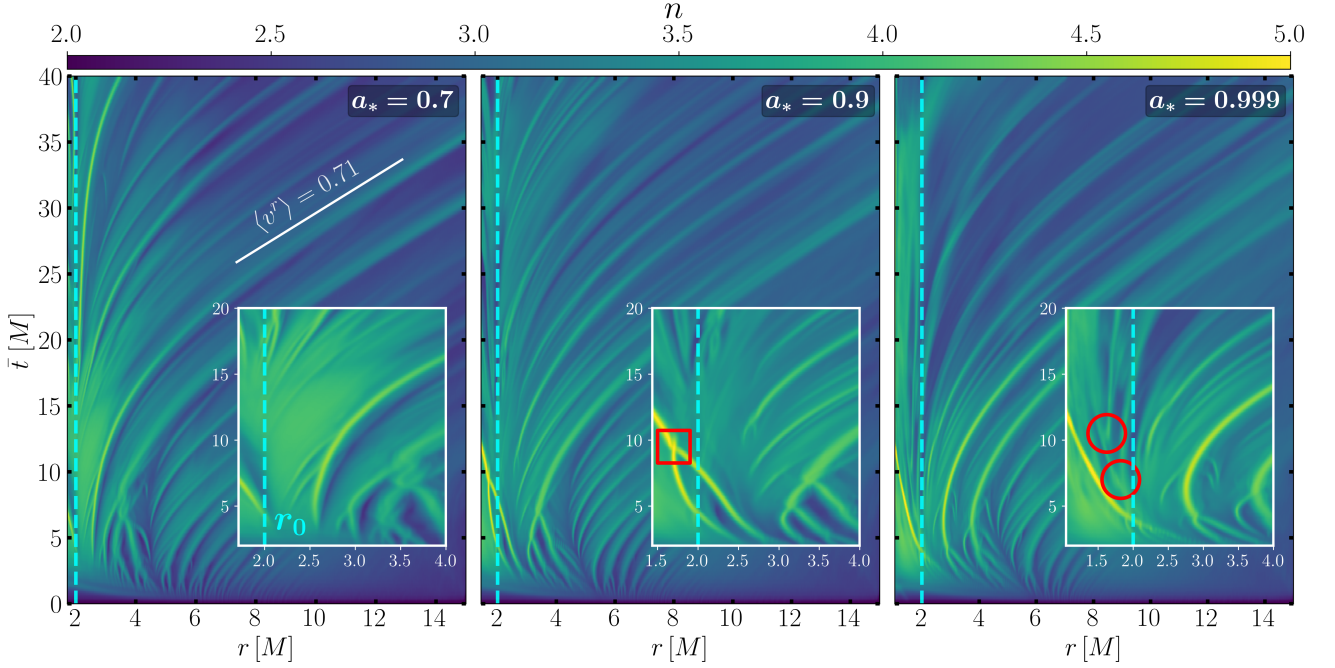


Figure 2: Spacetime diagrams of the total number density along the equatorial plane for BHs with spin $a_* = 0.7$ (left panel), $a_* = 0.9$ (middle panel), and $a_* = 0.999$ (right panel). The insets offer a magnification close to the event horizon and vertical dashed lines mark the location of the ergosphere r_0 . Peaks of the number density track the motion of the plasmoids, which can collide (red square) and split (red circles) within the ergosphere; outgoing plasmoids are accelerated at relativistic speeds $v^r \sim 0.7$ (see slope).

zeroes of the function $\mathcal{L}_{\text{ls}}(\Omega_f, r, \theta) := g_{\phi\phi}\Omega_f^2 + 2g_{t\phi}\Omega_f + g_{tt} = 0$ [11], where $g_{\mu\nu}$ is the background Kerr metric. The two zeros of $\mathcal{L}_{\text{ls}}(\Omega_f, r, \theta)$ mark the inner and outer light surfaces and are reported with blue solid lines in Fig. 1, with the former one being always located inside the ergoregion. Within the inner light surface, massive particles cannot corotate and acquire instead large radial infalling velocities at all latitudes, reaching Lorentz factors up to $\Gamma \sim 200$ and comparable to those observed for the particles accelerated by the magnetic reconnection along the equatorial plane (see below).

Another important surface reported in Fig. 1 is the so-called stagnation surface, that is, the surface with vanishing radial component of the three-velocity as measured from an asymptotic observer, $\langle v^r \rangle = 0$, where the brackets $\langle \rangle$ indicate the average of all the particles in a cell (the other components at the equatorial stagnation surface are $\langle v^\theta \rangle \sim 0.0$, $\langle v^\phi \rangle \sim 0.3$). We indicate it with a red solid line and note that it is open at very large distances, as expected with a plasma having a velocity component along the magnetic-field lines. Note also how its location on the equatorial plane is modified by the turbulent plasma dynamics resulting from reconnection and oscillates within the ergosphere. Occasionally, the stagnation surface moves very close to the event horizon, thus exposing large portions of the ergosphere where the plasma has $v^r > 0$ and can escape to large distances. Finally reported in the right panel of Fig. 1 is the distribution of the cell-averaged Lorentz factor as measured by the FIDO. As shown by the related colormap, the Lorentz factor is largest in the current sheet and associated with the plasmoids, that can reach velocities with $\Gamma \sim 100$.

To better illustrate and understand the dynamics of plasmoids, we present in Fig. 2, three spacetime diagrams for three representative high-spin BHs ($a_* = 0.7, 0.9, 0.999$ from left to right) over the time range $0 \leq \bar{t}/M \leq 40$. More specifically, we report the evolution in time of the total plasma density n along the current sheet (we average over a few cells around $\theta = \pi/2$ to minimise noise) and in the radial region $r_h \leq r \leq 15M$. Also shown with a cyan dashed line is the equatorial location of the ergosphere, $r_0 = 2M$, while the three insets report a magnification of the region close to the BH.

The spacetime diagrams clearly show the genesis of the plasmoids near the equatorial plane and their successive evolution either towards the horizon (leftwards trajectories), or to large distances (rightwards trajectories). Note also how small plasmoids can have binary mergers, sometimes multiple times (illustrated with a red square in the inset within the middle panel), and that these can happen either inside the ergosphere, or outside. In general, plasmoids that are born inside the ergoregion move towards the event horizon and fall into the BH with a

relatively small radial velocity. On the other hand, those born outside are ejected from the magnetosphere and accelerated to relativistic velocities. The use of a spacetime diagram allows us to trivially estimate the asymptotic velocities in terms of the slopes of the rightwards trajectories (see white line in leftmost panel of Fig. 2), from which we deduce that $\langle v^r \rangle \sim 0.7$. Remarkably, because this velocity appears to be essentially the same for all of the plasmoids and independently of the BH spin, it suggests that a steady wind of plasmoids with radial velocity $v^r \simeq 0.7$ should accompany the electrodynamics of plasma near BHs.

Importantly, note how in the case of the very rapidly spinning BH with $a_* = 0.999$ (rightmost panel in Fig. 2), and probably as a combination of tidal forces and extreme rotation, the spacetime diagram highlights the splitting of large plasmoids, leading to smaller plasmoids moving in opposite directions (see red circles in rightmost inset). While one plasmoid marches towards the event horizon, the other one seems to leave the ergosphere with a small radial velocity but a large azimuthal one. These conditions, that are present only in the ergosphere, are reminiscent of the conditions expected to lead to a Penrose process via magnetic reconnection [38–40]. While in our simulations this splitting has been measured only twice, this is, to the best of our knowledge, the first time that this process is shown to take place. Longer simulations are likely going to show more of these plasmoid-splittings, while larger particle numbers and higher spatial resolutions will help to better track the evolution of split plasmoids.

Rate of magnetic reconnection

One of the most important quantities characterising the dynamics of the force-free plasma we have simulated is given by the magnetic reconnection rate \mathcal{R} , which can be taken as the rate at which plasmoids are produced along the current sheet. We here estimate the reconnection rate in terms of the FIDO “drift velocity” defined as $V^i := \sqrt{\gamma} \eta^{ijk} D_j B_k / B^2$, where η^{ijk} is the Levi-Civita symbol. Using these quantities, we compute the reconnection rate as

$$\mathcal{R} := \frac{1}{2} \Delta V^\theta, \quad (1)$$

where ΔV^θ represents the jump in the polar drift velocity across the current sheet at the X-points where reconnection takes place on the equatorial plane. Also, we define the X-points as the regions where the radial profile of B^θ changes sign and which is located between two local maxima of the total number density taken to represent the plasmoids. We should remark that alternative measures are possible of the reconnection rate involving linear ratios of the electric and magnetic fields (see, e.g., [50–54]) and some authors also employ variants of Eq. (1) where FIDO and non-FIDO EM components are used [28, 47]. Overall, the different definitions are related and yield comparable estimates. Because \mathcal{R} exhibits a small but stochastic variation in time, we compute the averaged reconnection rate $\langle \mathcal{R} \rangle$ by sampling \mathcal{R} with a frequency in time of $1 M$ at all the X-points within a spatial bin of length $0.5 M$ on the equatorial plane, and then averaging over the total number of reconnection points contained in the bin.

Since the plasma dynamics is strongly influenced by the background spacetime, it is natural to expect that $\langle \mathcal{R} \rangle = \langle \mathcal{R} \rangle(a_*, r)$ [55]. As a result, in Fig. 3 we report the averaged reconnection rate $\langle \mathcal{R} \rangle$ as a function of spin and distance on the equatorial plane from the event horizon, $\mathcal{D} := r - r_h$. As expected from Figs. 1 and 2, the majority of reconnection events takes place near the BH and increases as a function of the spin. For any spin, the largest rate is always attained in the ergosphere (marked with a cyan dashed line) and reaches a maximum value of $\langle \mathcal{R} \rangle \sim 0.15$ for the maximally spinning BH considered with $a_* = 0.999$. Our results are in good agreement with other measurements of the reconnection rate in collisionless plasmas near BHs [28, 33, 47]. At a distance $\mathcal{D} \sim 7 M$ the reconnection rate has decreased to $\langle \mathcal{R} \rangle \simeq 0.02 - 0.03$, and becomes negligible at larger distances.

Given the regular behaviour of $\langle \mathcal{R} \rangle(a_*, r)$, it is possible to find a good analytic fit with the Ansatz

$$\mathcal{R}_{\text{fit}} = \frac{b_1(1 + b_2 M^2 \Omega_h^2)}{1 + b_3 r^2 / M^2}, \quad (2)$$

where the use of the angular frequency of the event-horizon $2M\Omega_h = a_*/(1 + \sqrt{1 - a_*^2})$ captures better than a_* the behaviour of the data. With fitting coefficients $b_1 = 0.183$, $b_2 = -0.361$, and $b_3 = 0.077$, we obtain a maximum relative error of $\lesssim 10\%$ for most of the fitting domain in Fig. 3.

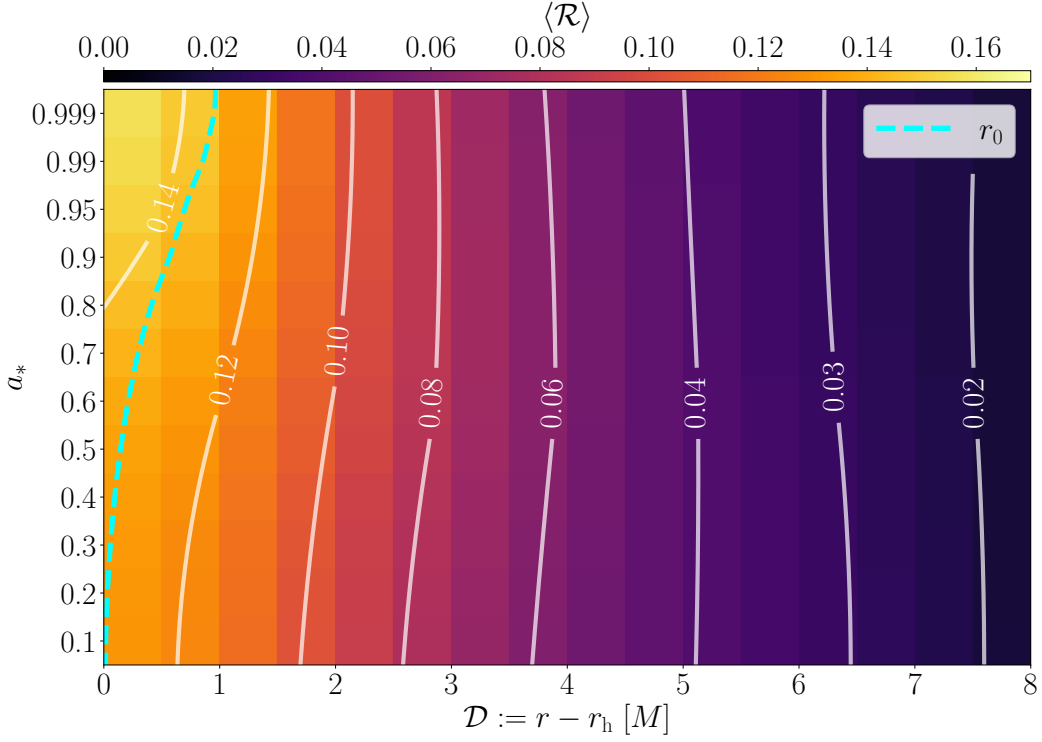


Figure 3: Averaged reconnection rate \mathcal{R} reported as a function of the spin a_* and the distance from the horizon \mathcal{D} . The average is computed in the time window $0 \leq \bar{t}/M \leq 40$ and with a spatial resolution of $0.5 M$. The cyan dashed line shows the position of the ergosphere r_0 for different BH spins.

Blandford-Znajek power

As anticipated, the BZ mechanism is an efficient process of conversion of the rotational energy into EM energy taking place when a force-free magnetosphere develops in BHs. As the preferred candidate mechanism to explain the power of relativistic jets in AGNs and GRBs, it plays a fundamental role in relativistic astrophysics. In what follows, we present the first measurements of the BZ luminosity from a fully kinetic GRPIC framework over the full range of the spin parameter. More specifically, we calculate the power emitted via the BZ mechanism in our split-monopole configuration by computing the Poynting flux over a two-sphere close to the BH horizon

$$P_{\text{BZ}} = \int (T^r_t)_{\text{EM}} \sqrt{-g} d\theta d\phi = 2\pi \int_0^\pi S^r \sqrt{\gamma} d\theta, \quad (3)$$

with \mathbf{T}_{EM} being the EM part of the energy-momentum tensor, $S^r := (E_\theta H_\phi - E_\phi H_\theta) / (4\pi \sqrt{\gamma})$ is the radial component of the Poynting vector, and \mathbf{H} the magnetic field measured by an asymptotic observer (see [Methods](#) for details). The (time-averaged) results of the GRPIC simulations are shown with black filled circles in Fig. 4, with the corresponding error-bars.

Already in the original work by Blandford and Znajek, an analytic expression was proposed to capture the dependence of the BZ power on the BH spin. Such a dependence can be expressed generically as

$$P_{\text{BZ}} = \frac{\kappa}{4\pi} \Phi_h^2 F(\Omega_h), \quad (4)$$

where Φ_h is the (half-hemisphere) magnetic flux and κ is a scaling factor independent of the BH spin and related to the topology of the magnetosphere; $\kappa_{sm} = 1/6\pi \approx 0.053$ for an ideal split-monopole magnetic field. The function $F(\Omega_h)$ in (4) expresses the spin-related contributions and for slowly-spinning BHs $F(\Omega_h) = \Omega_h^2 + \mathcal{O}(M^4 \Omega_h^4)$, so that the luminosity is given by the leading-order quadratic term originally derived by Blandford and Znajek, i.e., $P_{\text{BZ0}} := (\kappa_{sm}/4\pi) \Phi_h^2 \Omega_h^2 = (1/24\pi^2) \Phi_h^2 \Omega_h^2$ [1], and $P_{\text{BZ0}}^{\text{max}} \approx 10^{-3} (\Phi_h/M)^2$ represents the maximum value of the original BZ estimate attained for $M\Omega_h = 1/2$. Using analytic techniques that combine perturbation theory with a matched-asymptotic expansion scheme [8, 9], it was recently possible to obtain high-order corrections in $F(\Omega_h)$ up to $\mathcal{O}(\Omega_h^8)$ and expressed as

$$F_{\text{an}}(\Omega_h) = \Omega_h^2 \left[1 + \tilde{\alpha} (M\Omega_h)^2 + \tilde{\beta} (M\Omega_h)^4 + \tilde{\gamma} |M\Omega_h|^5 + \left(\tilde{\delta} + \tilde{\epsilon} \log |M\Omega_h| \right) (M\Omega_h)^6 \right] \mathcal{O}(M^9 \Omega_h^9). \quad (5)$$

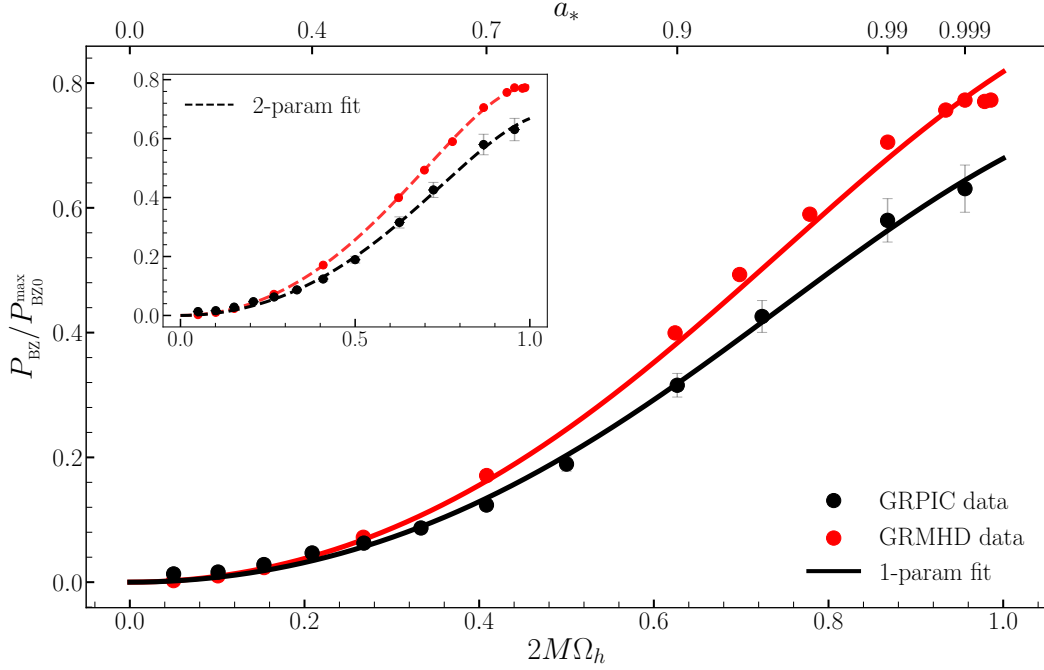


Figure 4: Blandford-Znajek luminosity P_{BZ} normalised to the maximum value of the lowest-order (i.e., quadratic) expression $P_{\text{BZ0}}^{\text{max}}$, as a function of the BH angular velocity (see top horizontal axis for a mapping in terms of the BH dimensionless spin) for all of our GRPIC simulations (black filled circles) and with the associated numerical errors. The black solid line shows the analytic expression (5) after rescaling the factor κ to account for the specific magnetic-field topology (one-parameter fit). Also reported are the data from GRMHD simulations [14] (red filled circles) and the corresponding analytic expression suitably rescaled for κ (red solid line). Shown in the inset with dashed lines of corresponding colours are the fits to the data in terms of the coefficients κ and $\tilde{\beta}$ (two-parameter fit).

where the coefficients in the expansion are given by $\tilde{\alpha} = 8(67 - 6\pi^2)/45 \simeq 1.38$ [4], $\tilde{\beta} \simeq -11.25$, $\tilde{\gamma} \simeq 1.54$, $\tilde{\delta} \simeq 11.64$, and $\tilde{\epsilon} \simeq 0.17$ [9].

Expression (4), with Φ_h computed as the time-averaged value of $1/2 \int |B^r| \sqrt{\gamma} d\theta d\phi$ at the horizon, and with the dependence (5) is reported as a black solid line in Fig. 4, where a one-parameter fit was made to fix the scaling factor $\kappa = 0.041$ since in our simulations the turbulent current sheet (slightly) distorts the magnetic-field topology away from an ideal split-monopole. Note how the analytic expression provides an excellent description of the GRPIC data at essentially all spins. To the best of our knowledge, this is the first time that the BZ power has been computed from kinetic simulations over the full range in spin and shown to be in very good agreement with the analytic prediction (see also [28] for a different magnetic-field configuration, with spin limited to $a_* \geq 0.6$, and P_{BZ} normalised to the initial magnetic flux). Importantly, the analytic expression fits very well also the data from two-dimensional GRMHD simulations [14] (red filled circles in Fig. 4), whose P_{BZ} values are systematically larger than the corresponding GRPIC ones (a result also found in [47]). For this data too, we have performed a one-parameter fit for the scaling factor $\kappa = 0.049$ (red solid line in Fig. 4). For both GRPIC and GRMHD data, the variance between the fit and the data is very small and is slightly better for the former dataset.

Following [14], who had access only to the quadratic coefficient $\tilde{\alpha}$ in expression (5), we show in the inset with corresponding colours and dashed lines the fits to the data when performing two-parameter fits for the coefficients κ and $\tilde{\beta}$, and thus truncating Eq. (5) at $\mathcal{O}(\Omega_h^6)$. Also in this case, the match with the data is extremely good and similar to that presented in Ref. [14]. Finally, we note that while we report error-bars for the GRPIC data of $\sim 6\%$, this is not done for the GRMHD data, as the errors are not available. However, we expect the data from GRMHD simulations to have similar if not larger errors (see, e.g., [47, 56]).

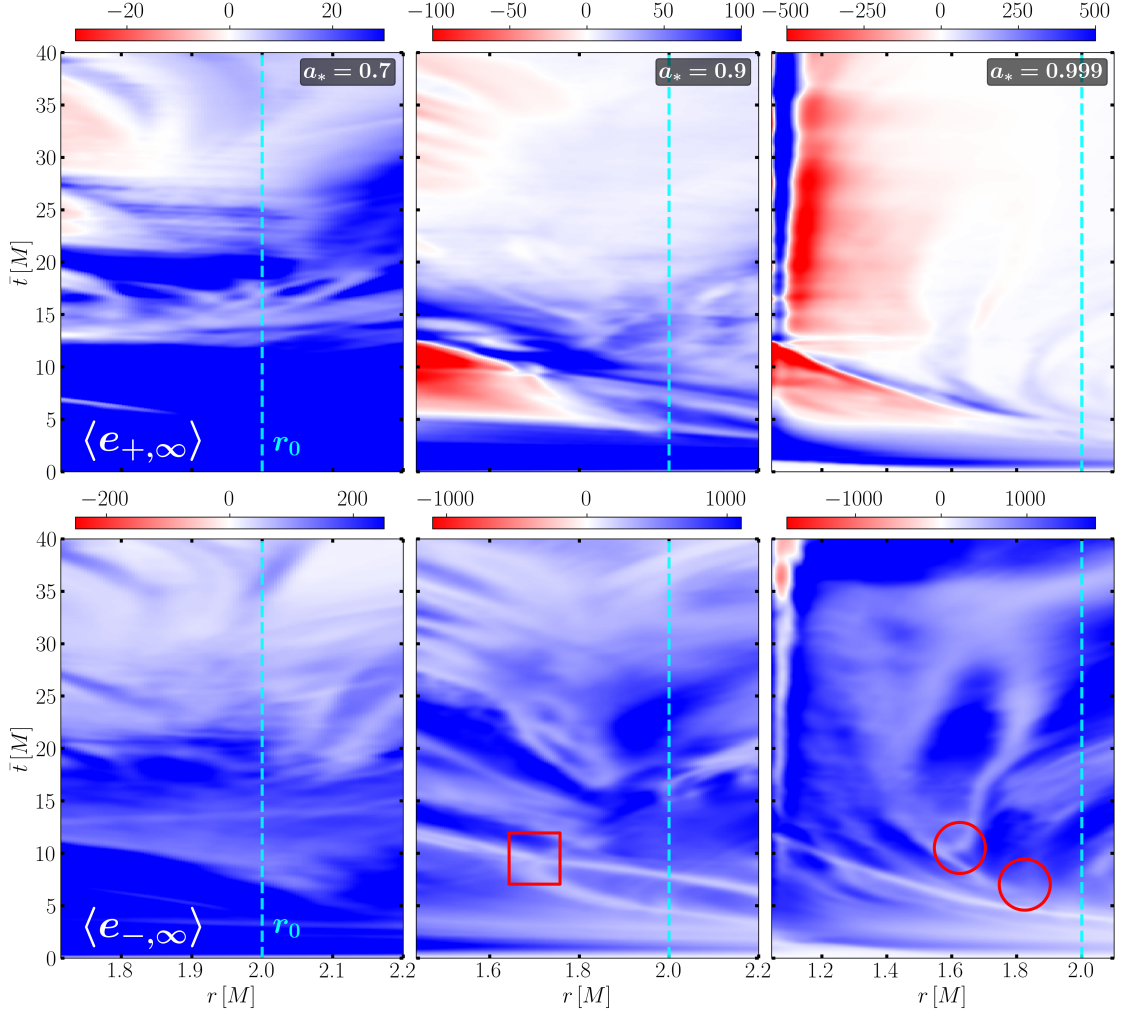


Figure 5: Spacetime diagrams for the average energy at infinity of positrons $\langle e_{+, \infty} \rangle$ (top row) and electrons $\langle e_{-, \infty} \rangle$ (bottom row) for the same simulations reported in Fig. 2. Note how negative-energy positrons are present even at moderate spins and their abundance and energies increases with the BH spin. In the case of electrons, only the highest spin leads to the generation of negative-energy electrons. As in Fig. 2, squares and circles are used to highlight the collision or splitting of plasmoids within the ergosphere.

Conditions for the Penrose process

We conclude the presentation of our results with a discussion on the particle energetics. Simulations with rapidly rotating BHs have revealed the presence of particles with negative energy at infinity, i.e., $e_\infty := -u_t < 0$, where u^μ is the particle’s four-velocity (see, e.g., [27–29, 57, 58]). Under these conditions, a Penrose process is possible whereby energy can be extracted from a Kerr BH when the negative-energy particles cross the event horizon [57]. In Fig. 5 we report spacetimes diagrams analogue to those shown in Fig. 2, but where we concentrate on the (averaged) energy at infinity of positrons, $\langle e_{+, \infty} \rangle$ (top row) and of electrons, $\langle e_{-, \infty} \rangle < 0$ (bottom row; note that the ranges differ from panel to panel). When focusing on the region close to the horizon and inside the ergosphere, that is, the only region where particles can show negative energies (red shading), it is simple to note that large spins are needed to produce particles with large negative energies and, indeed, the BH with $a_* = 0.7$ (left column) show particles with only moderate negative energies, while for the electrons $\langle e_{-, \infty} \rangle \gtrsim 0$ (blue shading).

On the other hand, for the extreme-spin BH with $a_* = 0.999$ (right column), the ergosphere is wider and a large population of positrons along the current sheet have negative energies. For $5 \lesssim \bar{t}/M \lesssim 13$ we observe a persistent region of negative-energy positrons near the horizon and entering it, thus suggesting that the Penrose process is active when a large plasmoid enters the BH (see rightmost panel of Fig. 1 around $\bar{t}/M \sim 10$). Inflow of negative-energy positrons can be seen very close to the event-horizon also later on, but this is not steady and restricted to a thin strip near the horizon. Note that at later times, i.e., $\bar{t}/M \gtrsim 35$, negative-energy electrons are produced near the event horizon and cross it, thus suggesting that also electrons represent a channel to extract energy from the BH. For less-extreme spins (middle column) this behaviour is less pronounced, but negative-energy positrons are still present at different times, with smaller negative energies matching the smaller BH rotational energy, while no negative-energy electrons appear over the timescale of our simulations. Overall, these results – including the distinct behaviour of electrons and positrons – are in good agreement with those presented in Ref. [27], where lower asymptotic energies were reported for the positrons and electrons.

Interestingly, when associating the trajectories of plasmoids with those of the concentrations of the number density (as done in Fig. 2), such trajectories actually refer mostly to electrons with zero energies at infinity and are surrounded by regions with $\langle e_{+, \infty} \rangle < 0$ or $\langle e_{+, \infty} \rangle > 0$. This is particularly clear in the right panel of the top row and suggests that in their propagation plasmoids “leak” positrons of either negative or positive energy at infinity. This is the case also for the splitting-plasmoids discussed in Fig. 2 and whose locations we report also in the right panel of the bottom row with red circles. Also in this case, in fact, the plasmoid trajectory is accompanied by regions of positrons with positive and negative energies. While this behaviour is intriguing, simulations with higher-resolution in particle number at extremal spins, that are presently prohibitive, may be needed to reveal the complex relation between plasmoid motion and the production of negative-energy particles.

Discussion

Exploiting a newly developed general-relativistic kinetic code, we have carried out the most comprehensive campaign of first-principle GRPIC simulations of a classical scenario in relativistic astrophysics: a rotating BH threaded by a split-monopole magnetic field. This configuration is well-known to lead to the generation of a current sheet near the equatorial plane and to magnetic reconnection, responsible for the production of chains of relativistic plasmoids. Because they offer a global view on the electrodynamics of BHs ranging from slowly rotating ones over to BH near the extremal limit, our simulations have allowed us to obtain a number of novel results.

First, we have been able to follow both in space and time the dynamics of the plasmoids generated in the current sheet and to illustrate how they either move towards the BH and are accreted or escape at large distances at radial velocities $v^r \simeq 0.7$ for all BH spins. The study of spacetime diagrams has also highlighted that plasmoids can collide and generate larger ones, but also split if present in the ergosphere, thus resembling the conditions expected to lead to a Penrose process via magnetic reconnection. Second, using the large set of simulations, we have been able to compute the reconnection rate under different conditions and express it in terms of the BH spin and the distance from the event horizon. The behaviour found for the reconnection rate is regular and can be represented by an analytic function that can be used in analytic models of magnetic reconnection in BH spacetimes. Third, we have measured the power associated with the Blandford-Znajek mechanism and found excellent agreement with the high-order predictions coming from perturbation theory. The match, which

requires the calculation of a single coefficient independent of the BH spin and related to the specific magnetic-field topology, works equally well with data from GRMHD simulations. To the best of our knowledge, this is the first time that both GRPIC and GRMHD simulations of the BZ mechanism are shown to be compatible with the analytic predictions and can be rescaled via a single coefficient. Finally, the use of the spacetime diagrams and the analysis of the plasmoids near the current sheet has highlighted that negative-energy particles can be created inside the ergosphere and be accreted by the BH, thus potentially leading to a Penrose process. While positrons are much more likely to yield to negative-energy trajectories, which are activated already at moderately high spins $a_* \simeq 0.7$ and are abundant for $a_* \simeq 0.999$, also electrons have been found to have negative energies for the most extreme spins. These results suggest therefore that the electrodynamics of a rotating BH with a split-monopole field may be responsible for both a BZ mechanism and a Penrose process.

While the results presented here are exciting and offer motivation for a number of follow-up studies, we should also remark on some of their limitations. First, they are restricted to two spatial dimensions as this is the only route to afford high-resolution and long-term simulations over a large range of BH spins. Clearly, a much richer dynamics is to be expected when this analysis will be extended to three dimensions. Second, while the particle and spatial resolution employed here are large and sufficient to reach consistency in the results, some finer details, such as those associated with the splitting of plasmoids, would benefit from even more accurate calculations to address, for instance, the properties of the negative-energy and outgoing plasmoid. Finally, the physical conditions near a BH are surely more complex than those represented here in terms of a pure pair-plasma. In addition to electrons and positrons, in fact, protons and ions will be present and a full multi-species description is necessary to study their dynamics. We plan to address at least some of these aspects with future work.

Methods

In what follows we provide additional details on a number of aspects of our analysis that we have omitted in the main text for compactness.

Numerical Setup

We have performed GRPIC simulations using the newly developed Frankfurt code `FPIC`, which models the dynamics of charged particles in a stationary and axisymmetric spacetime described by the Kerr metric with a dimensionless spin parameter $0 \leq a_* \leq 1$. The simulations are performed in 2.5 dimensions, i.e., in conditions where the particles have motions in three spatial dimensions and the EM fields have three spatial components but are evolved in a two-dimensional domain in response to the underlying axisymmetry of the background spacetime [59]. More specifically, when considering a spherical coordinate system (r, θ, ϕ) and the BH spin axis to be along the $\theta = 0$ coordinate line, we assume invariance in the azimuthal direction, so that $\partial_\phi \psi = 0$ for all quantities ψ in the code.

To ensure regularity of the spacetime metric at the BH horizon, the Kerr metric is expressed in terms of the spherical Kerr-Schild coordinates (t, r, θ, ϕ) adopting a $3 + 1$ decomposition. In this way, both the particles and the EM fields are evolved with respect to the proper time of FIDOs, whose worldlines are orthogonal to the constant- t slices [11, 60]. The line element is thus given by $ds^2 = -\alpha^2 dt^2 + \gamma_{ij}(dx^i + \beta^i dt)(dx^j + \beta^j dt)$, with α and β^i respectively being the lapse function and the shift vector (see, e.g., [61] for explicit expressions of α , β , and γ).

The EM fields are evolved according to the relativistic Maxwell-Faraday and Maxwell-Ampere equations [62]

$$\partial_t \mathbf{B} = -\nabla \times (\alpha \mathbf{D} + \boldsymbol{\beta} \times \mathbf{B}), \quad (6)$$

$$\partial_t \mathbf{D} = \nabla \times (\alpha \mathbf{B} - \boldsymbol{\beta} \times \mathbf{D}) - 4\pi \mathbf{J}, \quad (7)$$

with the auxiliary current $\mathbf{J} := \alpha \mathbf{j} - \rho \boldsymbol{\beta}$, and where ρ , \mathbf{j} , \mathbf{B} and \mathbf{D} represent respectively the (total) electric charge and current densities, as well as the magnetic and electric fields measured by the FIDOs. The EM fields as measured by an asymptotic observer can always be recovered from FIDO EM fields via the transformations

$$\mathbf{E} = \alpha \mathbf{D} + \boldsymbol{\beta} \times \mathbf{B}, \quad (8)$$

$$\mathbf{H} = \alpha \mathbf{B} - \boldsymbol{\beta} \times \mathbf{D}. \quad (9)$$

The divergence-free condition for the magnetic field is preserved by means of the staggered Yee grid, which ensures that $\partial_j(\sqrt{\gamma}B^j)/\sqrt{\gamma} \sim 0$ up to the machine round-off error [63]. Note that when solving Eqs. (6)–(9), the EM field components are interpolated onto the same grid position via a metric-weighted linear interpolation. In addition, we enforce the Maxwell-Gauss law for the electric field by applying a divergence-cleaning approach [53, 64] in which we employ an iterative Jacobi method with 500 iterations and update the corrected electric field via Eq. (6) every 25 timesteps. In this way, we can ensure that $\|\partial_j(\sqrt{\gamma}D^j)/\sqrt{\gamma} - 4\pi\rho\|_\infty/\|4\pi\rho\|_\infty \lesssim 10^{-3}$.

The general-relativistic equations of motion for the position and four-velocity of the charged particles are given respectively by (for completeness we restore here the speed of light)

$$\frac{1}{c} \frac{dx^i}{dt} = \frac{\alpha}{\Gamma} \gamma^{ij} u_j - \beta^i, \quad (10)$$

$$\frac{1}{c} \frac{du_i}{dt} = -\Gamma \partial_i \alpha + u_j \partial_i \beta^j - \frac{\alpha}{2\Gamma} u_l u_m \partial_i \gamma^{lm} + \frac{q\alpha}{mc^2} \left[\gamma_{ij} D^j + \frac{\sqrt{\gamma} \eta_{ijk} \gamma^{jl} u_l B^k}{\Gamma} \right], \quad (11)$$

where $\Gamma := \sqrt{1 + \gamma^{ij} u_i u_j}$ is the particles Lorentz factor measured by a FIDO, m is the mass of the particles, and $q = \pm e$ the charge.

FPIC implements three different schemes to solve Eqs. (10)–(11): an explicit fourth-order Runge-Kutta (RK) integrator, a classical Boris scheme [65], and a second-order implicit Hamiltonian method [66]. The latter is the most accurate one but also computationally, while the Boris and the RK schemes shown very similar results in terms of accuracy at a fraction of the computational cost. As a results, although the RK integrator is not symplectic, i.e., the area of a given region of the phase space is not guaranteed to be preserved over long timescales, (as required by Liouville’s theorem [61]), it has represented for us the optimal approach in terms of accuracy and computational costs. Note also that, at least for the Kerr spacetimes considered here, both the metric components in Eqs. (10)–(11) and their derivatives are computed analytically at the position of the particle. After updating the positions and velocities of the particles, the charge and current densities computed from the sources are moved to the Yee grid via a metric-weighted 2D linear interpolation.

Particles reaching the outer boundary or falling into the BH are removed from the ensemble, while they are reflected when passing across the poles for axisymmetry (i.e., with u_θ changing sign at the poles). As a result, new particles need to be introduced to compensate for these losses and maintain high the particle number density. We perform the injection of new particles every $\Delta t_{\text{inj}} = 0.01 M$ and only for those cells for which the multiplicity condition $\mathcal{M} < 10$ is satisfied. The chosen values for the frequency of injection and for the multiplicity are adequate to fill the magnetosphere with $n \gg n_{\text{GJ}}$ (see Fig. 1) without impacting the speed of the simulations. Overall, the number of particles evolved at every time-step can reach $N_p \simeq 3 \times 10^8$ for the most extreme spin values (see Tab. 1). Finally, the time-step Δt is set by the Courant-Friedrichs-Lewy (CFL) condition and given, in two dimensions, by $\Delta t = \mathcal{C}[\beta^r/\Delta r + \alpha\sqrt{\gamma^{rr}/\Delta r^2 + \gamma^{\theta\theta}/\Delta\theta^2}]^{-1}$, where $\mathcal{C} = 0.5$ is the CFL coefficient.

For each simulation, whose main properties are summarised in Tab. 1, the axisymmetric computational domain starts from within the event horizon, thus in a region causally disconnected from the rest of the domain, and covers a radial extent $0.95 r_h \leq r \leq 20 M$ and a polar one $1/200 \leq \theta/\pi \leq 199/200$ via $N_r \times N_\theta = 4196 \times 1024$ cells. An additional outer layer with absorbing boundary conditions for the EM fields is applied at $r_{\text{abs}} := 0.9 r_{\text{max}} = 18 M$. In this layer, resistive terms are added to Maxwell equations to damp the EM fields and ensure that the reflection of EM waves at the outer boundary does not affect the inner computational domain [67].

Acknowledgements

We thank Luca Comisso and Ileyk El Mellah for insightful comments on the manuscript, and Alejandro Cruz-Orsorio for useful discussions during the development of the code. Support comes from the ERC Advanced Grant “JETSET: Launching, propagation and emission of relativistic jets from binary mergers and across mass scales” (Grant No. 884631). L. R. acknowledges the Walter Greiner Gesellschaft zur Förderung der physikalischen Grundlagenforschung e.V. through the Carl W. Fueck Laureatus Chair. The simulations were performed on the local ITP Supercomputing Clusters Iboga and Calea, on the Goethe-HLR supercomputer, and on HPE Apollo HAWK at the High Performance Computing Center Stuttgart (HLRS) under the grant BNSMIC.

Table 1: Table of GRPIC simulations. Starting from the top, we report: the name of the Run, the dimensionless spin parameter a_* , the angular velocity Ω_h , the event horizon radius r_h , the Goldreich-Julian density n_{GJ} , the normalised injected number density n_0/n_{GJ} , and the total number of particles N_p evolved at $t \sim 90 M$, expressed in millions.

Simulation	a.1	a.2	a.3	a.4	a.5	a.6	a.7	a.8	a.9	a.95	a.99	a.999
a_*	0.1	0.2	0.3	0.4	0.5	0.6	0.7	0.8	0.9	0.95	0.99	0.999
$\Omega_h [M^{-1}]$	0.03	0.05	0.07	0.10	0.13	0.17	0.20	0.25	0.31	0.36	0.43	0.47
$r_h [M]$	1.99	1.98	1.95	1.92	1.87	1.80	1.71	1.60	1.44	1.31	1.14	1.04
$n_{\text{GJ}} [M^{-3}]$	2.0	4.0	6.1	8.3	10.7	13.3	16.2	19.9	24.9	28.8	34.5	38.0
n_0/n_{GJ}	5.00	2.50	1.64	1.20	0.93	0.75	0.61	0.50	0.40	0.35	0.29	0.26
$N_p/10^6$	37	61	82	106	127	157	182	211	256	268	289	312

References

- [1] R. D. Blandford and R. L. Znajek, “Electromagnetic extraction of energy from Kerr black holes,” *Mon. Not. R. Astron. Soc.*, vol. 179, pp. 433–456, May 1977.
- [2] M. A. Abramowicz and P. C. Fragile, “Foundations of black hole accretion disk theory,” *Living Rev. Relativity*, vol. 16, no. 1, 2013.
- [3] K. S. Thorne and D. Macdonald, “Electrodynamics in curved spacetime: 3+1 formulation,” *Mon. Not. R. Astr. Soc.*, vol. 198, pp. 339–343, 1982.
- [4] K. Tanabe and S. Nagataki, “Extended monopole solution of the Blandford-Znajek mechanism: Higher order terms for a Kerr parameter,” *Phys. Rev. D*, vol. 78, p. 024004, 2008.
- [5] V. S. Morozova, L. Rezzolla, and B. J. Ahmedov, “Nonsingular electrodynamics of a rotating black hole moving in an asymptotically uniform magnetic test field,” *Phys. Rev. D*, vol. 89, p. 104030, May 2014.
- [6] J.-P. Lasota, E. Gourgoulhon, M. Abramowicz, A. Tchekhovskoy, and R. Narayan, “Extracting black-hole rotational energy: The generalized Penrose process,” *Phys. Rev. D*, vol. 89, p. 024041, Jan. 2014.
- [7] S. Kinoshita and T. Igata, “The essence of the Blandford–Znajek process,” *PTEP*, vol. 2018, no. 3, p. 033E02, 2018.
- [8] J. Armas, Y. Cai, G. Compère, D. Garfinkle, and S. E. Gralla, “Consistent Blandford-Znajek Expansion,” *JCAP*, vol. 04, p. 009, 2020.
- [9] F. Camilloni, O. J. C. Dias, G. Grignani, T. Harmark, R. Oliveri, M. Orselli, A. Placidi, and J. E. Santos, “Blandford-Znajek monopole expansion revisited: novel non-analytic contributions to the power emission,” *JCAP*, vol. 07, no. 07, p. 032, 2022.
- [10] S. S. Komissarov, “Direct numerical simulations of the Blandford-Znajek effect,” *Mon. Not. R. Astron. Soc.*, vol. 326, pp. L41–L44, Sept. 2001.
- [11] S. S. Komissarov, “Electrodynamics of black hole magnetospheres,” *Mon. Not. R. Astron. Soc.*, vol. 350, pp. 427–448, May 2004.
- [12] J. C. McKinney and C. F. Gammie, “A measurement of the electromagnetic luminosity of a Kerr black hole,” *Astrophys. J.*, vol. 611, p. 977, 2004.
- [13] S. S. Komissarov, “Observations of the Blandford-Znajek process and the magnetohydrodynamic Penrose process in computer simulations of black hole magnetospheres,” *Mon. Not. R. Astron. Soc.*, vol. 359, pp. 801–808, May 2005.
- [14] A. Tchekhovskoy, R. Narayan, and J. C. McKinney, “Black Hole Spin and The Radio Loud/Quiet Dichotomy of Active Galactic Nuclei,” *Astrophys. J.*, vol. 711, pp. 50–63, Mar. 2010.

- [15] A. Tchekhovskoy, R. Narayan, and J. C. McKinney, “Efficient generation of jets from magnetically arrested accretion on a rapidly spinning black hole,” *Mon. Not. R. Astron. Soc.*, vol. 418, pp. L79–L83, Nov. 2011.
- [16] L. Rezzolla, B. Giacomazzo, L. Baiotti, J. Granot, C. Kouveliotou, and M. A. Aloy, “The Missing Link: Merging Neutron Stars Naturally Produce Jet-like Structures and Can Power Short Gamma-ray Bursts,” *Astrophys. J. Letters*, vol. 732, p. L6, May 2011.
- [17] M. Ruiz, C. Palenzuela, F. Galeazzi, and C. Bona, “The role of the ergosphere in the Blandford-Znajek process,” in *Mon. Not. R. Astron. Soc.*, p. 2851, Apr. 2012.
- [18] R. F. Penna, R. Narayan, and A. Sadowski, “General Relativistic Magnetohydrodynamic Simulations of Blandford-Znajek Jets and the Membrane Paradigm,” *arXiv:1307.4752*, July 2013.
- [19] A. Nathanail and I. Contopoulos, “Black Hole Magnetospheres,” *Astrophys. J.*, vol. 788, p. 186, June 2014.
- [20] K. Akiyama and *et al.*, “First M87 Event Horizon Telescope Results. I. The Shadow of the Supermassive Black Hole,” *Astrophys. J. Lett.*, vol. 875, p. L1, Apr. 2019.
- [21] K. Akiyama and *et al.*, “First M87 Event Horizon Telescope Results. V. Physical Origin of the Asymmetric Ring,” *Astrophys. J. Lett.*, vol. 875, p. L5, Apr. 2019.
- [22] A. Nathanail, A. Stranzalis, and I. Contopoulos, “The rapid decay phase of the afterglow as the signature of the Blandford-Znajek mechanism,” *Mon. Not. R. Astron. Soc.*, vol. 455, pp. 4479–4486, Feb. 2016.
- [23] O. Gottlieb, A. Lalakos, O. Bromberg, M. Liska, and A. Tchekhovskoy, “Black hole to breakout: 3D GRMHD simulations of collapsar jets reveal a wide range of transients,” *Mon. Not. Roy. Astron. Soc.*, vol. 510, no. 4, pp. 4962–4975, 2022.
- [24] Event Horizon Telescope Collaboration, K. Akiyama, *et al.*, “First Sagittarius A* Event Horizon Telescope Results. I. The Shadow of the Supermassive Black Hole in the Center of the Milky Way,” *Astrophys. J. Lett.*, vol. 930, p. L12, May 2022.
- [25] Event Horizon Telescope Collaboration, K. Akiyama, *et al.*, “First Sagittarius A* Event Horizon Telescope Results. V. Testing Astrophysical Models of the Galactic Center Black Hole,” *Astrophys. J. Lett.*, vol. 930, p. L16, May 2022.
- [26] M. Shibata, S. Fujibayashi, A. T.-L. Lam, K. Ioka, and Y. Sekiguchi, “Outflow energy and black-hole spin evolution in collapsar scenarios,” *Phys. Rev. D*, vol. 109, no. 4, p. 043051, 2024.
- [27] K. Parfrey, A. Philippov, and B. Cerutti, “First-Principles Plasma Simulations of Black-Hole Jet Launching,” *Phys. Rev. Lett.*, vol. 122, p. 035101, Jan. 2019.
- [28] I. El Mellah, B. Cerutti, B. Crinquand, and K. Parfrey, “Spinning black holes magnetically connected to a Keplerian disk. Magnetosphere, reconnection sheet, particle acceleration, and coronal heating,” *Astron. Astrophys.*, vol. 663, p. A169, July 2022.
- [29] K. Hirotani, R. Krasnopolsky, H. Shang, K.-i. Nishikawa, and M. Watson, “Two-dimensional Particle-in-cell Simulations of Axisymmetric Black Hole Magnetospheres,” *Astrophys. J.*, vol. 908, p. 88, Feb. 2021.
- [30] R. Torres, T. Grismayer, F. Cruz, R. A. Fonseca, and L. O. Silva, “OSIRIS-GR: General relativistic activation of the polar cap of a compact neutron star,” *Nature*, vol. 112, p. 102261, Nov. 2024.
- [31] Y. Yuan, A. Y. Chen, and M. Luepker, “Physics of Pair-producing Gaps in Black Hole Magnetospheres: Two-dimensional General Relativistic Particle-in-cell Simulations,” *Astrophys. J.*, vol. 985, p. 159, June 2025.
- [32] A. Y. Chen, M. Luepker, and Y. Yuan, “Introducing APERTURE: A GPU-based General Relativistic Particle-in-Cell Simulation Framework,” *arXiv e-prints*, p. arXiv:2503.04558, Mar. 2025.

- [33] B. Crinquand, B. Cerutti, G. Dubus, K. Parfrey, and A. Philippov, “Synthetic images of magnetospheric reconnection-powered radiation around supermassive black holes,” *Phys. Rev. Lett.*, vol. 129, p. 205101, Nov 2022.
- [34] B. Ripperda, M. Liska, K. Chatterjee, G. Musoke, A. A. Philippov, S. B. Markoff, A. Tchekhovskoy, and Z. Younsi, “Black Hole Flares: Ejection of Accreted Magnetic Flux through 3D Plasmoid-mediated Reconnection,” *Astrophys. J. Lett.*, vol. 924, p. L32, Jan. 2022.
- [35] D. A. Uzdensky, “The Fast Collisionless Reconnection Condition and the Self-Organization of Solar Coronal Heating,” *Astroph. J.*, vol. 671, pp. 2139–2153, Dec. 2007.
- [36] A. Bhattacharjee, Y.-M. Huang, H. Yang, and B. Rogers, “Fast reconnection in high-Lundquist-number plasmas due to the plasmoid instability,” *Physics of Plasmas*, vol. 16, p. 112102, Nov. 2009.
- [37] R. Penrose and R. M. Floyd, “Extraction of Rotational Energy from a Black Hole,” *Nature Physical Science*, vol. 229, pp. 177–179, Feb. 1971.
- [38] F. A. Asenjo and L. Comisso, “Generalized magnetofluid connections in relativistic magnetohydrodynamics,” *Phys. Rev. Lett.*, vol. 114, p. 115003, Mar 2015.
- [39] L. Comisso and F. A. Asenjo, “Magnetic reconnection as a mechanism for energy extraction from rotating black holes,” *Phys. Rev. D*, vol. 103, p. 023014, Jan 2021.
- [40] F. Camilloni and L. Rezzolla, “Self-consistent Multidimensional Penrose Process Driven by Magnetic Reconnection,” *Astrophys. J. Lett.*, vol. 982, p. L31, Mar. 2025.
- [41] S. E. Gralla and T. Jacobson, “Spacetime approach to force-free magnetospheres,” *Mon. Not. Roy. Astron. Soc.*, vol. 445, no. 3, pp. 2500–2534, 2014. [Erratum: *Mon. Not. Roy. Astron. Soc.* 534, 1541 (2024)].
- [42] P. Goldreich and W. H. Julian, “Pulsar Electrodynamics,” *Astrophys. J.*, vol. 157, p. 869, Aug. 1969.
- [43] R. M. Wald, “Black hole in a uniform magnetic field,” *Phys. Rev. D*, vol. 10, pp. 1680–1685, Sept. 1974.
- [44] P. Mösta, C. Palenzuela, L. Rezzolla, L. Lehner, S. Yoshida, and D. Pollney, “Vacuum Electromagnetic Counterparts of Binary Black-Hole Mergers,” *Phys. Rev. D*, vol. 81, p. 064017, 2010.
- [45] D. Alic, P. Moesta, L. Rezzolla, O. Zanotti, and J. L. Jaramillo, “Accurate Simulations of Binary Black Hole Mergers in Force-free Electrodynamics,” *Astrophys. J.*, vol. 754, p. 36, July 2012.
- [46] V. S. Beskin, “Axisymmetric stationary flows in compact astrophysical objects,” *Soviet Physics Uspekhi*, vol. 40, pp. 659–688, July 1997.
- [47] A. Bransgrove, B. Ripperda, and A. Philippov, “Magnetic Hair and Reconnection in Black Hole Magnetospheres,” *Phys. Rev. Lett.*, vol. 127, p. 055101, July 2021.
- [48] Z. R.L., “Black hole electrodynamics and the carter tetrad,” *Mon. Not. R. Astron. Soc.*, vol. 80, no. 2, p. 024032, 1977.
- [49] D. A. Uzdensky, “Force-Free Magnetosphere of an Accretion Disk-Black Hole System. II. Kerr Geometry,” *Astrophys. J.*, vol. 620, pp. 889–904, Feb. 2005.
- [50] S. Zenitani and M. Hoshino, “The generation of nonthermal particles in the relativistic magnetic reconnection of pair plasmas,” *Astrophys. J.*, vol. 562, no. 1, p. L63, 2001.
- [51] D. Kagan, L. Sironi, B. Cerutti, and D. Giannios, “Relativistic Magnetic Reconnection in Pair Plasmas and Its Astrophysical Applications,” *Space Science Reviews*, vol. 191, pp. 545–573, Oct. 2015.
- [52] Y.-H. Liu, F. Guo, W. Daughton, H. Li, and M. Hesse, “Scaling of magnetic reconnection in relativistic collisionless pair plasmas,” *Phys. Rev. Lett.*, vol. 114, p. 095002, Mar 2015.

- [53] B. Crinquand, B. Cerutti, G. Dubus, K. Parfrey, and A. Philippov, “Synthetic gamma-ray light curves of Kerr black hole magnetospheric activity from particle-in-cell simulations,” *Astron. Astrophys.*, vol. 650, p. A163, June 2021.
- [54] M. Imbrogno, C. Meringolo, A. Cruz-Osorio, L. Rezzolla, B. Cerutti, and S. Servidio, “Turbulence and Magnetic Reconnection in Relativistic Multi-Species Plasmas,” *arXiv e-prints*, p. arXiv:2505.09700, May 2025.
- [55] F. A. Asenjo and L. Comisso, “Relativistic Magnetic Reconnection in Kerr Spacetime,” *Phys. Rev. Lett.*, vol. 118, no. 5, p. 055101, 2017.
- [56] Event Horizon Telescope Collaboration, O. Porth, *et al.*, “The Event Horizon General Relativistic Magnetohydrodynamic Code Comparison Project,” *Astrophys. J. Supp.*, vol. 243, p. 26, Aug. 2019.
- [57] R. Penrose, “Gravitational collapse: The role of general relativity,” *Riv. Nuovo Cimento*, vol. 1, p. 252, 1969.
- [58] R. F. Penna, “Energy extraction from boosted black holes: Penrose process, jets, and the membrane at infinity,” *Phys. Rev. D*, vol. 91, p. 084044, Apr. 2015.
- [59] C. Meringolo and L. Rezzolla, “FPIC: the Frankfurt particle-in-cell code for stationary and axisymmetric black-hole spacetimes,” 2025. in preparation.
- [60] D. Macdonald and K. S. Thorne, “Black-hole electrodynamics: an absolute-space/universal formulation,” *Mon. Not. Roy. Astron. Soc.*, vol. 198, pp. 345–382, 1982.
- [61] L. Rezzolla and O. Zanotti, *Relativistic Hydrodynamics*. Oxford: Oxford University Press, 9 2013.
- [62] S. S. Komissarov, “General relativistic mhd simulations of monopole magnetospheres of black holes,” *Mon. Not. R. Astron. Soc.*, vol. 350, p. 1431, 2004.
- [63] K. Yee, “Numerical solution of initial boundary value problems involving maxwell’s equations in isotropic media,” *IEEE Transactions on Antennas and Propagation*, vol. 14, pp. 302–307, May 1966.
- [64] C. K. Birdsall and A. B. Langdon, *Plasma Physics via Computer Simulation (Reprinted)*. 2005.
- [65] J. P. Boris and D. L. Book, “Flux-corrected transport. I. SHASTA, a fluid transport algorithm that works,” *J. Comput. Phys.*, vol. 11, no. 1, pp. 38–69, 1973.
- [66] F. Bacchini, B. Ripperda, A. Y. Chen, and L. Sironi, “Generalized, Energy-conserving Numerical Simulations of Particles in General Relativity. I. Time-like and Null Geodesics,” *Astrophys. J., Supp.*, vol. 237, p. 6, July 2018.
- [67] B. Cerutti, A. Philippov, K. Parfrey, and A. Spitkovsky, “Particle acceleration in axisymmetric pulsar current sheets,” *Mon. Not. R. Astron. Soc.*, vol. 448, pp. 606–619, Mar. 2015.